

RESEARCH ARTICLE | JULY 21 2023

Resonant and non-resonant flows in longitudinally and latitudinally librating spheres

Special Collection: [Precession, Nutation, and Libration Driven Flows](#)

Yufeng Lin (林玉峰) ; Rainer Hollerbach ; Jérôme Noir  ; Stijn Vantieghem 



Physics of Fluids 35, 076612 (2023)

<https://doi.org/10.1063/5.0142705>



View
Online



Export
Citation

[CrossMark](#)

Resonant and non-resonant flows in longitudinally and latitudinally librating spheres

Cite as: Phys. Fluids **35**, 076612 (2023); doi: [10.1063/5.0142705](https://doi.org/10.1063/5.0142705)

Submitted: 16 January 2023 · Accepted: 14 April 2023 ·

Published Online: 21 July 2023



View Online



Export Citation



CrossMark

Yufeng Lin (林玉峰),^{1,a)}  Rainer Hollerbach,^{2,3,a)}  Jérôme Noir,^{4,a),b)}  and Stijn Vantieghem^{4,c)} 

AFFILIATIONS

¹Department of Earth and Space Sciences, Southern University of Science and Technology, Shenzhen 518055, People's Republic of China

²Department of Applied Mathematics, University of Leeds, Leeds LS2 9JT, United Kingdom

³Isaac Newton Institute for Mathematical Sciences, 20 Clarkson Road, Cambridge CB3 0EH, United Kingdom

⁴Institut für Geophysik, Sonneggstrasse 5, ETH Zürich, Zürich CH-8092, Switzerland

Note: This paper is part of the special topic, Precession, Nutation, and Libration Driven Flows.

^{a)}J. Noir, Y. Lin, and R. Hollerbach would like to honor the memory of S. Vantieghem by dedicating this work to him. Sadly, S. Vantieghem passed away just three days after the paper was accepted for publication.

^{b)}Author to whom correspondence should be addressed: jerome.noir@erdw.ethz.ch

^{c)}Deceased.

ABSTRACT

We investigate the linear response to longitudinal and latitudinal libration of a rapidly rotating fluid-filled sphere. Asymptotic methods are used to explore the structure of resonant modes in both cases, provided that the nondimensional libration frequency is in the range $\omega \in [0, 2]$. High-resolution numerics are then used to map out this entire frequency range, picking out both the resonant peaks as well as the non-resonant troughs in between. The kinetic energy is independent of the Ekman number E at the peaks and scales as $E^{1/2}$ at the troughs. As the Ekman number is reduced, down to $E = 10^{-10}$ for longitudinal libration and $E = 10^{-9}$ for latitudinal libration, the frequency response also exhibits an increasingly fractal structure, with more and more peaks and troughs emerging. The spacing between peaks is seen to follow an $E^{1/2}$ self-similarity factor. However, detailed examinations of some of the more prominent troughs shows that their widths follow an $E^{-0.23}$ self-similarity factor.

© 2023 Author(s). All article content, except where otherwise noted, is licensed under a Creative Commons Attribution (CC BY) license (<http://creativecommons.org/licenses/by/4.0/>). <https://doi.org/10.1063/5.0142705>

I. INTRODUCTION

Many planetary satellites undergo a phenomenon called libration. This term refers to a harmonic oscillation of the boundary of a rotating body with respect to its mean spin axis. One can distinguish between two types of librations: east–west and north–south oscillations are referred to as librations in longitude and latitude, respectively (see Fig. 1). Another distinction can be made based on the physical mechanism giving rise to the librations. First, forced librations are caused by time-dependent gravitational torques that are exerted on an orbiting planet or moon. The forced longitudinal librations arise from the tidal bulge resulting from a low spin–orbit resonance and an eccentric orbit leading to a time-dependent orbital velocity, i.e., Kepler's third law.^{1,2} The periodic misalignment of the bulge generates an axial torque, leading to a harmonic oscillation of the rotation rate of the planets and moons around their mean value, as illustrated in Fig. 2(a). Forced

latitudinal librations are due to the obliquity of the orbit combined with the polar flattening of the mantle, leading to an equatorial torque that tends to realign the equator of the planets or moons with their orbital planes. As a result, the celestial objects exhibit a small oscillation along an equatorial axis that is fixed in the frame rotating with the body, see Fig. 2(b). Second, free librations both in longitude and latitude may follow from a large impact; in such a case the oscillations are expected to decay over time due to dissipation both in the solid and liquid shells. Note also that nutations and polar motion can be thought of as types of latitudinal librations, and variations in length of day can be thought of as a type of longitudinal libration, although in all these cases the frequencies involved are much smaller than for the librations we are interested in.

Starting with the pioneering work of Poincaré,⁴ many scientists have used observations of changes in the spin rate of a planet or moon

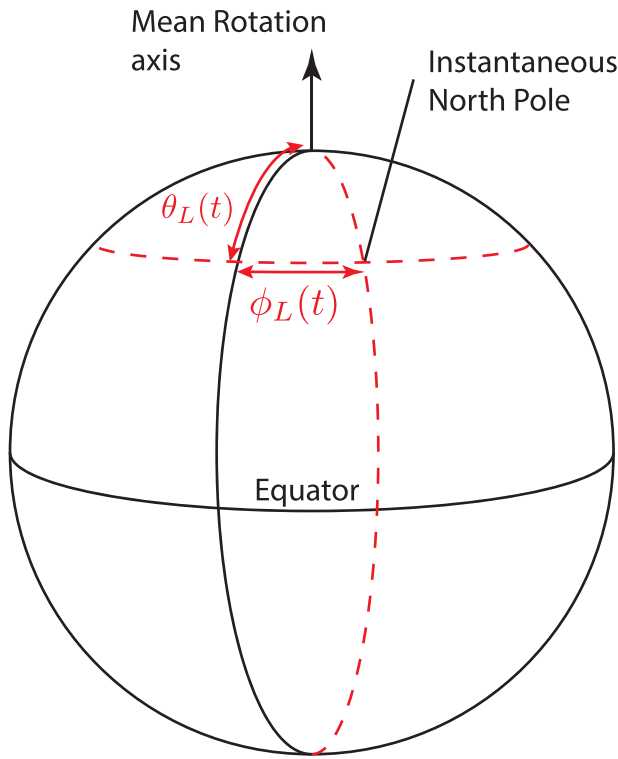


FIG. 1. Illustrative sketch of longitudinal and latitudinal librations, denoted, respectively, by angles $\phi_L(t)$ and $\theta_L(t)$.

to infer its interior structure. In most of these studies, the couplings between fluid and solid parts of a planet are often simplified under the *ad hoc* assumption that the fluid is essentially behaving as a rigidly rotating solid body. Testing the validity of this approach requires detailed fluid mechanical investigation of the response of a fluid body to a change in the rotation of its overlaying mantle. Roughly speaking, one can identify three physical mechanisms that can transmit the motion of the mantle to the fluid: (i) topographic coupling due to a deviation of sphericity, (ii) viscous coupling emanating from the core–mantle boundary, and (iii) electromagnetic coupling in the presence of a magnetic field and if the mantle is electrically conducting (at least weakly).

The first fluid mechanical investigations of libration-driven flows in spherical enclosures were carried out by Greenspan⁵ and Aldridge and Toomre,⁶ who used a theoretical and experimental approach, respectively, to study the linear response of the fluid to longitudinal libration forcing (see also Ref. 7). Later studies have addressed the genesis of boundary-layer instabilities, the presence of an inner shell, and the zonal flows produced by nonlinear effects.^{8–16} As far as topographic coupling is concerned, most studies have focused on the instabilities and turbulence that ensue from an elliptical or higher-order multipolar deformation of the boundary.^{17–20} For a general discussion, we refer also to the two reviews on precession, libration and tidally driven flows, Le Bars *et al.*²¹ and Chap. 4 of Le Bars and Lecoanet.²²

Much less attention has been devoted to flows driven by libration in latitude. References 23 and 24 investigated the spheroidal geometry and found that a topographic resonance can occur when the libration frequency matches the eigenfrequency of the spin-over inertial mode.

This was extended toward triaxial ellipsoids by Ref. 25, who also investigated parametric instabilities driven by the shear and strain induced by the ellipsoidal geometry.

In this work, we focus on viscous coupling mechanisms. Using theoretical and numerical methods, we study both longitudinal and latitudinal libration-driven flows in the limit of vanishing viscosity and small forcing amplitude. First, we introduce the governing equations in Sec. II. In Sec. III, we use the classical boundary layer theory of Greenspan to compute the linear response of the fluid to the libration forcing; in Secs. IV and V, we compare our theoretical results against high-resolution numerical simulations.

II. GOVERNING EQUATIONS

We consider a homogeneous, incompressible fluid enclosed within a sphere of radius R that is undergoing libration. The mean rotation axis of the cavity points in the z -direction, and the mean rotation rate is Ω_0 . We will adopt the convention that for latitudinal libration, the libration axis is parallel to the x -direction. In a frame of reference that is attached to the librating sphere, the so-called mantle frame, the Navier–Stokes equation becomes

$$\frac{\partial \mathbf{u}}{\partial t} + \mathbf{u} \cdot \nabla \mathbf{u} + 2\mathbf{\Omega} \times \mathbf{u} + \rho^{-1} \nabla p = \nu \nabla^2 \mathbf{u} + \mathbf{r} \times \dot{\mathbf{\Omega}} \quad (1)$$

together with the associated incompressibility condition $\nabla \cdot \mathbf{u} = 0$ that will apply to all flows throughout this paper. Here, \mathbf{u} , t , p , ρ , and ν denote the velocity field, time, pressure, mass density, and kinematic viscosity, respectively. The last term on the right-hand side of Eq. (1) is termed the Poincaré acceleration and is a consequence of the non-inertial character of the librating mantle frame. The total rotation vector $\mathbf{\Omega}$ is given by

$$\mathbf{\Omega} = (0, 0, \Omega_0 + \dot{\phi}_L), \quad (2)$$

$$\mathbf{\Omega} = (\dot{\theta}_L, \Omega_0 \sin \theta_L, \Omega_0 \cos \theta_L), \quad (3)$$

for longitudinal and latitudinal libration, respectively, where $\dot{\phi}_L$ denotes the time derivative of ϕ_L , the instantaneous east–west displacement of the sphere with respect to the mean rotation axis, and similarly $\dot{\theta}_L$ denotes the time derivative of θ_L , the instantaneous inclination with respect to the mean rotation axis. More precisely, we have

$$\phi_L(t) = \Delta\phi \sin(\omega t), \quad \theta_L(t) = \Delta\theta \sin(\omega t), \quad (4)$$

where $\Delta\phi$ and $\Delta\theta$ are the amplitudes and ω is the libration frequency.

It is customary to write the equations in non-dimensional form. Adopting Ω_0^{-1} as a timescale and R as a length scale, we find

$$\frac{\partial \mathbf{u}}{\partial t} + \mathbf{u} \cdot \nabla \mathbf{u} + 2\mathbf{\Omega} \times \mathbf{u} + \nabla p = E \nabla^2 \mathbf{u} + \mathbf{r} \times \dot{\mathbf{\Omega}}. \quad (5)$$

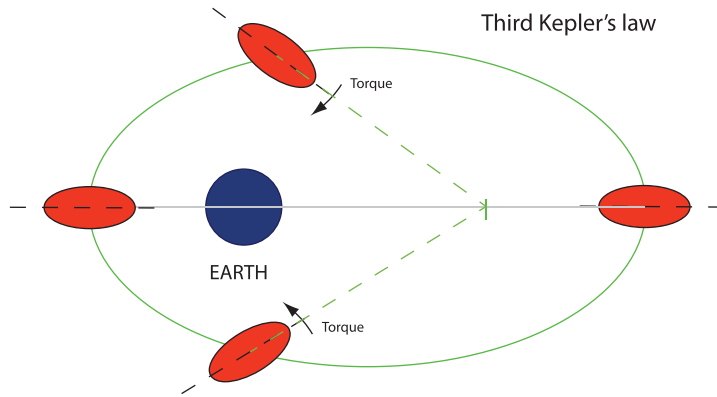
Here, we introduce the Ekman number E ,

$$E = \frac{\nu}{\Omega_0 R^2}. \quad (6)$$

Another non-dimensional parameter governing the problem is the Poincaré number $\varepsilon_{\phi, \theta}$, which measures the strength of the Poincaré acceleration with respect to the Coriolis acceleration,

$$\varepsilon_{\phi} = \frac{\Delta\phi \omega}{\Omega_0}, \quad \varepsilon_{\theta} = \frac{\Delta\theta \omega}{\Omega_0}. \quad (7)$$

a) Longitudinal libration:



b) Latitudinal libration:

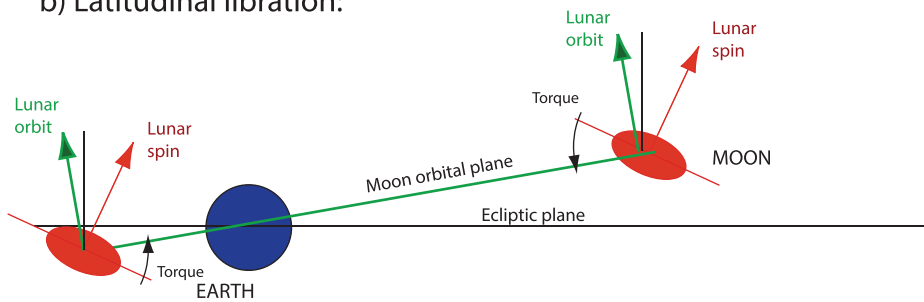


FIG. 2. Mechanisms giving rise to librations in longitude (a) and latitude (b). Shown are the host body, its satellite at different positions along its orbital trajectory, and the gravitational torques resulting from variations in the orbital speed (a) and a non-alignment between the lunar spin and its orbital plane (b). This figure has been adapted from Vantieghem *et al.*³

The major rationale for using the mantle frame is that the boundary conditions at the surface of the sphere are particularly simple,

$$\mathbf{u}_\Sigma = \mathbf{0}. \tag{8}$$

Nevertheless, it will also be instructive to write down the equations with respect to the frame of reference of mean rotation, i.e., a reference frame that is rotating at (constant) rate Ω_0 with respect to the inertial frame. The Navier–Stokes equation is then

$$\frac{\partial \mathbf{u}}{\partial t} + \mathbf{u} \cdot \nabla \mathbf{u} + 2\hat{\mathbf{z}} \times \mathbf{u} + \nabla p = E \nabla^2 \mathbf{u}, \tag{9}$$

and the corresponding boundary conditions are

$$\mathbf{u}_\Sigma = \varepsilon_\phi \cos(\omega t) \mathbf{r} \times \hat{\mathbf{z}}, \tag{10}$$

$$\mathbf{u}_\Sigma = \varepsilon_\theta \cos(\omega t) \mathbf{r} \times \hat{\mathbf{x}} \tag{11}$$

for longitudinal and latitudinal libration, respectively.

III. ASYMPTOTIC LINEAR THEORY

In the context of planetary physics, the non-dimensional parameters take typical values $10^{-8} \lesssim \varepsilon_{\theta,\phi} \lesssim 10^{-4}$, $10^{-15} \lesssim E \lesssim 10^{-10}$, and $\omega \approx 1$, with the exception of Mercury for which $\omega \approx 2/3$. The smallness of the parameters $\varepsilon_{\theta,\phi}$ and E justifies the use of the asymptotic linear theory as developed by Greenspan²⁶ and Zhang and Liao.²⁷ In the

rest of the paper, we follow a similar approach to these authors recalling the important steps. We perform asymptotic analysis in the reference frame of mean rotation following Greenspan,²⁶ while Zhang and Liao²⁷ used the mantle frame for the asymptotic theory. We, thus, focus on the linearized equations of motion, expressed with respect to the frame of mean rotation,

$$\frac{\partial \mathbf{u}}{\partial t} + 2\hat{\mathbf{z}} \times \mathbf{u} + \nabla p = E \nabla^2 \mathbf{u}. \tag{12}$$

We write the solution $\{\mathbf{u}, p\}$ in terms of an asymptotic series of the form

$$\mathbf{u} = \varepsilon_{\theta,\phi} [\mathbf{u}_0 + \tilde{\mathbf{u}} + E^{1/2} \hat{\mathbf{u}} + \dots] e^{i\omega t}, \tag{13}$$

$$p = \varepsilon_{\theta,\phi} [p_0 + \tilde{p} + E^{1/2} \hat{p} + \dots] e^{i\omega t}, \tag{14}$$

with the term between brackets being a function of the space coordinate \mathbf{r} only. Since Eq. (12) is linear, the solution will have the same harmonic time-dependence as the forcing. The quantities \mathbf{u}_0 and p_0 are the leading-order solutions within the interior of the sphere, whereas $\tilde{\mathbf{u}}$ and \tilde{p} denote boundary layer quantities that are asymptotically small everywhere except in the Ekman layer of thickness $O(E^{1/2})$ near the boundary. As it will turn out, this Ekman layer drives a small

mass flux into the interior region, the so-called Ekman pumping, with related quantities $\hat{\mathbf{u}}$ and \hat{p} .

Within the interior, viscous forces are of order of magnitude E and can be neglected at leading order. The leading order interior solution is, thus, governed by the system

$$i\omega \mathbf{u}_0 + 2\hat{\mathbf{z}} \times \mathbf{u}_0 + \nabla p_0 = 0, \tag{15}$$

subject to the boundary condition

$$\mathbf{u}_0 \cdot \hat{\mathbf{r}}|_{r=1} = 0. \tag{16}$$

It has been shown that any sufficiently smooth flow field that satisfies the impermeability condition in full spheres and ellipsoids can be expanded in a series of inertial modes.^{28,29} Based on this result, we decompose the velocity \mathbf{u}_0 and the pressure p_0 in terms of inertial modes as follows:

$$\mathbf{u}_0 = \sum_{lmk} A_{lmk} \mathbf{u}_{lmk}, \quad p_0 = \sum_{lmk} A_{lmk} p_{lmk}, \tag{17}$$

where \mathbf{u}_{lmk} and p_{lmk} are solutions of

$$i(\omega - \omega_{lmk}) \mathbf{u}_{lmk} + 2\hat{\mathbf{z}} \times \mathbf{u}_{lmk} + \nabla p_{lmk} = 0 \tag{18}$$

subject to the boundary condition $\mathbf{u}_{lmk} \cdot \hat{\mathbf{r}}|_{r=1} = 0$. The indices l and m refer to spherical harmonic degree and order; k corresponds to the radial eigenfunctions. Further properties of these analytically obtainable inertial modes in spherical enclosures are discussed in Appendix A.

By substituting the expansions (17) into (15), taking the inner product with \mathbf{u}_{lmk} , integrating over the sphere and making use of the orthogonality property (A8) of inertial modes, we obtain

$$i(\omega - \omega_{lmk}) A_{lmk} = 0. \tag{19}$$

Hence, the coefficient A_{lmk} vanishes at the leading order of approximation, except if the libration frequency ω equals the eigenfrequency ω_{lmk} . Inertial mode eigenfrequencies being restricted to the interval $\omega_{lmk} \in [0, 2]$, and being dense within this interval, we can conclude the following:

1. If the libration frequency $\omega \geq 2$, A_{lmk} is necessarily 0, which implies that it is not possible to drive an $O(1)$ flow.
2. If, on the other hand, $\omega < 2$, it may be possible to excite an inertial mode whose eigenfrequency matches the libration frequency. The modal amplitudes A_{lmk} , however, cannot be found directly from Eq. (19), but, as we shall see in the next paragraphs, require taking into account viscous effects, reflecting the purely viscous nature of the coupling between the fluid and the shell.

We now focus on the latter case, and include the Ekman pumping contribution into the interior solution. As such, we obtain

$$i \sum_{lmk} A_{lmk} (\omega - \omega_{lmk}) \mathbf{u}_{lmk} + i\omega \hat{\mathbf{u}} + 2\hat{\mathbf{z}} \times \hat{\mathbf{u}} + \nabla \hat{p} = 0, \tag{20}$$

with inhomogeneous boundary condition

$$\hat{\mathbf{u}} \cdot \hat{\mathbf{r}}|_{r=1} = \Phi_{Ekman}, \tag{21}$$

where Φ_{Ekman} denotes the (radial) mass flux associated with the Ekman pumping. This quantity is directly related to the non-zero ‘‘horizontal divergence’’ of the boundary-layer solution,

$$\begin{aligned} \Phi_{Ekman} &= E^{1/2} \int_0^\infty \nabla_\perp \cdot \tilde{\mathbf{u}} \, d\zeta \\ &= E^{1/2} \int_0^\infty \left[\frac{1}{\sin \theta} \frac{\partial}{\partial \theta} (\tilde{u}_\theta \sin \theta) + \frac{1}{\sin \theta} \frac{\partial}{\partial \phi} \tilde{u}_\phi \right] d\zeta, \end{aligned} \tag{22}$$

where $\zeta = E^{-1/2}(1 - r)$ is a stretched boundary-layer coordinate.

Finding the boundary layer flow that matches a given interior flow \mathbf{u}_0 to the non-slip boundary condition (10)–(11) is a rather classical problem²⁶ that we discuss in detail in Appendix B. The final result is

$$\tilde{\mathbf{u}} = \tilde{\mathbf{u}}_+ \exp(\gamma_+ \zeta) + \tilde{\mathbf{u}}_- \exp(\gamma_- \zeta), \tag{23}$$

with

$$\gamma_+ = -\frac{\sqrt{2}}{2} \left(1 + i \frac{\omega + 2 \cos \theta}{|\omega + 2 \cos \theta|} \right) |\omega + 2 \cos \theta|^{1/2}, \tag{24}$$

$$\gamma_- = -\frac{\sqrt{2}}{2} \left(1 + i \frac{\omega - 2 \cos \theta}{|\omega - 2 \cos \theta|} \right) |\omega - 2 \cos \theta|^{1/2}, \tag{25}$$

and

$$\tilde{\mathbf{u}}_+ = \frac{1}{2} (A_{lmk} (\mathbf{u}_{lmk} - i\hat{\mathbf{r}} \times \mathbf{u}_{lmk}) - (\mathbf{u}_\Sigma - i\hat{\mathbf{r}} \times \mathbf{u}_\Sigma)), \tag{26}$$

$$\tilde{\mathbf{u}}_- = \frac{1}{2} (A_{lmk} (\mathbf{u}_{lmk} + i\hat{\mathbf{r}} \times \mathbf{u}_{lmk}) - (\mathbf{u}_\Sigma + i\hat{\mathbf{r}} \times \mathbf{u}_\Sigma)). \tag{27}$$

We see that the boundary layer solution contains both terms proportional to the interior flow $A_{lmk} \mathbf{u}_{lmk}$ and terms proportional to \mathbf{u}_Σ , given by Eq. (10) or (11). From Eq. (22), it follows that the Ekman pumping will also depend on $A_{lmk} \mathbf{u}_{lmk}$ and \mathbf{u}_Σ . As will be shown next, this can be used to determine the unknown amplitudes A_{lmk} .

To this end, we take the inner product of (20) with \mathbf{u}_{lmk} , integrating over the surface of the sphere and performing integration by parts to obtain

$$\int p_{lmk}^\dagger \Phi_{Ekman} \, d\Sigma = i(\omega - \omega_{lmk}) \left[A_{lmk} + \int \int \int \hat{\mathbf{u}} \cdot \mathbf{u}_{lmk}^\dagger \, dV \right], \tag{28}$$

where \dagger denotes complex conjugation. Provided that $(\omega - \omega_{lmk}) \ll E^{1/2}$, the right-hand side of this expression vanishes at order $E^{1/2}$. This yields the so-called solvability condition,

$$\int p_{lmk}^\dagger \Phi_{Ekman} \, d\Sigma = 0, \tag{29}$$

where the integral is taken over the surface of the sphere. By combining Eqs. (29), (22), (10), (11), and (23)–(27), it can be shown that, after a considerable amount of algebra, this leads to

$$A_{lmk} = \frac{\int \nabla p_{lmk}^\dagger \cdot [\gamma_+^{-1} (\mathbf{u}_\Sigma - i\hat{\mathbf{r}} \times \mathbf{u}_\Sigma) + \gamma_-^{-1} (\mathbf{u}_\Sigma + i\hat{\mathbf{r}} \times \mathbf{u}_\Sigma)] \, d\Sigma}{\int \nabla p_{lmk}^\dagger \cdot [\gamma_+^{-1} (\mathbf{u}_{lmk} - i\hat{\mathbf{r}} \times \mathbf{u}_{lmk}) + \gamma_-^{-1} (\mathbf{u}_{lmk} + i\hat{\mathbf{r}} \times \mathbf{u}_{lmk})] \, d\Sigma}, \tag{30}$$

where the coefficients γ^\pm are a function of θ only and are given by (24) and (25). Given a triplet of indices $\{l, m, k\}$, Eq. (30) permits the computation of the modal amplitude A_{lmk} given a driving frequency $\omega = \omega_{lmk}$. Since longitudinal and latitudinal libration are

TABLE I. Longitudinal libration: comparison of the normalized kinetic energy at the frequencies of the lowest-order modes obtained from the asymptotic theory, E_{lmk}/ϵ_ϕ^2 , and from high-resolution linear numerical simulations at $E = 10^{-8}$, E_{num}/ϵ_ϕ^2 . In the last column we also report the values given by Zhang and Liao.²⁷

(m, l, k)	ω_{lmk}	S_{lmk}	E_{lmk}/ϵ_ϕ^2	E_{num}/ϵ_ϕ^2	E_{ZL}/ϵ_ϕ^2
(0,4,1)	1.309 307 341	0.426 775 579 0	$4.437\ 333\ 386 \times 10^{-2}$	4.421×10^{-2}	4.440×10^{-2}
(0,6,1)	0.937 697 587	0.318 769 489 4	$2.852\ 976\ 237 \times 10^{-2}$	2.834×10^{-2}	2.848×10^{-2}
(0,6,2)	1.660 447 793	0.555 430 038 4	$8.244\ 384\ 738 \times 10^{-3}$	8.009×10^{-3}	7.959×10^{-3}
(0,8,1)	1.799 515 990	0.610 750 963 0	$2.289\ 522\ 846 \times 10^{-3}$	2.252×10^{-3}	...
(0,8,2)	0.726 234 926	0.253 129 413 2	$1.827\ 816\ 203 \times 10^{-2}$	1.834×10^{-2}	...
(0,8,3)	1.354 372 557	0.471 011 105 6	$9.463\ 982\ 745 \times 10^{-3}$	9.649×10^{-3}	...

characterized, respectively, by an $m = 0$ and $m = 1$ azimuthal dependency, it follows from (30) that these mechanisms can only drive modes with azimuthal wavenumbers $m = 0$ and $m = 1$. Taking into account the expression (A4) for the pressure eigenmode at the spherical surface, the θ component of ∇p_{lmk} is of parity $(l - m - 1)$ with respect to the equator, and the ϕ component is of parity $(l - m)$. Combining this with the specific symmetry of the boundary forcing, we come to the conclusion that the numerator of (30) vanishes if l is odd. In other words, both longitudinal and latitudinal libration can only drive modes for which l is even.

To compare our results to the high-resolution numerical simulations discussed in Sec. VB, we define the normalized total kinetic energy in a sphere of unit radius stored in a forced inertial mode (l, m, k) :

$$E_{lmk}/\epsilon_{\phi,\theta}^2 = \frac{1}{2} \int \int \int \frac{|A_{lmk}|^2}{\epsilon_{\phi,\theta}^2} \mathbf{u}_{lmk} \cdot \mathbf{u}_{lmk}^\dagger dV. \quad (31)$$

Note that in the calculation of the kinetic energy, we exclude the contributions from the Ekman boundary layer and the so-called conical shear layers that spawn from the critical latitude, which contributions to the total kinetic energy are of order $E^{1/2}$ and $E^{3/5}$, respectively.

In Tables I and II, we provide kinetic energy obtained for a libration frequency $\omega = \omega_{lmk}$, both by evaluating (30) and (31) for the mode (l, m, k) , and by means of high-resolution numerical simulations. For comparison, we also present the values of the kinetic energy from Zhang and Liao²⁷ (p. 243); noticing that their kinetic energy is volume-averaged, their results must also be multiplied by $4\pi/3$, and

one should only account for the mode contribution and not the apparent fluid motion due to their choice to look at the dynamics from the mantle frame of reference. For instance, the kinetic energy for the mode at $\omega = 1.3093$, labeled (0, 1, 2) in Zhang and Liao²⁷ and (0, 4, 1) with our conventions, the kinetic energy in their manuscript is

$$\bar{E}_{kin}/Po^2 = \left[\frac{1}{10} + 0.0106 \right],$$

whereas with our notations and conventions, we obtain for this mode

$$E_{ZL}/\epsilon_\phi^2 = \frac{4\pi}{3} \times 0.0106.$$

Our results and Zhang and Liao are in quantitative agreement, as expected from the similarity of the derivation but for the choice of frame of reference. Zhang and Liao²⁷ also treated latitudinal librations only in spheroids rather than spheres, so no direct comparison with our results is available in that case. We find that the amplitude of the kinetic energy at the peak is effectively independent of the Ekman number, and in particular, there is no divergence of the amplitude of the modes as the Ekman number vanishes, in agreement with Refs. 7 and 27.

To go beyond the first order approximation, we account for the viscous correction to the inviscid eigen-frequency S_{lmk} derived by Greenspan²⁶ such that $\omega_{lmk}(E) = \omega_{lmk} + S_{lmk}E^{1/2}$, also reported in Tables I and II. Note that Zhang and Liao²⁷ did not consider the viscous correction to the eigen-frequency, whereas Greenspan²⁶ considered both the real and imaginary parts of the viscous correction to the

TABLE II. Latitudinal libration: comparison of the normalized kinetic energy at the frequencies of the lowest-order modes obtained from the asymptotic theory, $E_{lmk}/\epsilon_\theta^2$, and from high-resolution linear numerical simulations at $E = 10^{-8}$, $E_{num}/\epsilon_\theta^2$.

(m, l, k)	ω_{lmk}	S_{lmk}	$E_{lmk}/\epsilon_\theta^2$	$E_{num}/\epsilon_\theta^2$
(1,2,1)	1.000 000 000	0.258 463 392 8	$2.094\ 395\ 103 \times 10^{-1}$	2.097×10^{-1}
(1,4,1)	1.708 023 904	0.504 571 758 0	$4.869\ 232\ 497 \times 10^{-2}$	4.827×10^{-2}
(1,4,2)	0.820 008 840	0.316 519 274 5	$7.972\ 175\ 759 \times 10^{-3}$	1.015×10^{-2}
(1,4,3)	0.611 984 936	0.180 786 895 0	$3.807\ 897\ 735 \times 10^{-2}$	3.867×10^{-2}
(1,6,1)	0.440 454 452	0.138 816 148 5	$1.465\ 674\ 965 \times 10^{-2}$	1.408×10^{-2}
(1,6,2)	1.306078717	0.429 554 895 2	$2.188\ 323\ 255 \times 10^{-2}$	2.198×10^{-2}
(1,6,3)	1.861 684 240	0.560 603 944 5	$1.724\ 853\ 435 \times 10^{-2}$	1.736×10^{-2}
(1,6,4)	0.537 333 891	0.202 556 729 8	$5.284\ 148\ 108 \times 10^{-3}$	5.706×10^{-3}
(1,6,5)	1.404 216 852	0.526 006 866 5	$7.314\ 363\ 353 \times 10^{-4}$	1.005×10^{-3}

eigen-frequency. Nevertheless, the viscous correction of $O(E^{1/2})$ to the inviscid eigen-frequency only produces small discrepancies in the total energy as we can see from Table I.

IV. NUMERICAL METHOD

Numerical calculations are done in the mean rotation frame, with Eq. (12) the equation to be solved. Making the replacement $\frac{\partial}{\partial t} = i\omega$, this becomes

$$i\omega \mathbf{u} + 2\hat{\mathbf{z}} \times \mathbf{u} + \nabla p - E\nabla^2 \mathbf{u} = 0. \quad (32)$$

The incompressibility condition $\nabla \cdot \mathbf{u} = 0$ is fulfilled by taking the toroidal–poloidal decomposition,

$$\mathbf{u} = \nabla \times (e \hat{\mathbf{r}}) + \nabla \times \nabla \times (f \hat{\mathbf{r}}). \quad (33)$$

The scalar quantities e and f are expanded in terms of associated Legendre functions as

$$e = \sum_{n=1}^N e_n(r) P_{2n-1}^{(m)}(\cos \theta) e^{im\phi} e^{i\omega t}, \quad (34)$$

$$f = \sum_{n=1}^N f_n(r) P_{2n}^{(m)}(\cos \theta) e^{im\phi} e^{i\omega t}, \quad (35)$$

where $m = 0, 1$ for longitudinal and latitudinal libration, respectively. Inserting Eq. (33) into (32), taking the r -components of the first and second curls of Eq. (32), and using properties of the associated Legendre functions then yields a block tri-diagonal matrix structure,^{30,31} where each block contains the details of the radial expansion.

For this radial expansion, we follow the full-sphere approach of Ref. 32 and expand in terms of Chebyshev polynomials $T_k(x)$ as

$$e_n(r) = \sum_{k=1}^K e_{nk} T_{2k-1}(x) r, \quad f_n(r) = \sum_{k=1}^K f_{nk} T_{2k-1}(x) r^2. \quad (36)$$

Using only the odd Chebyshev polynomials, as well as the additional factors r and r^2 ensures that the leading-order regularity conditions at the origin are satisfied. The difference between r for e vs r^2 for f is due to the odd vs even Legendre functions in Eqs. (34) and (35), which induces different symmetries in r , as shown, for example, in the appendix of Ref. 33. The Chebyshev variable x and the actual radial coordinate r are related by either $r = x$, or a slightly more complicated formula discussed below.

The boundary conditions associated with Eq. (32) are Eqs. (10) or (11) as before, except that the previous amplitude factors $\Delta\epsilon_\phi$ and $\Delta\epsilon_\theta$ are now absent since the problem is linear. Working through the details, and recalling also that the $\cos(\omega t)$ factors there are already accounted for by the $e^{i\omega t}$ factors here, the final result is remarkably simple, namely, just $e_1(1) = 1$, for both longitudinal and latitudinal libration. For all other modes, the original no-slip boundary conditions on \mathbf{u} convert to simply $e_n = f_n = f'_n = 0$.

The original equation and its associated boundary conditions therefore convert to a matrix problem $\mathbf{A}\mathbf{v} = \mathbf{b}$, where \mathbf{A} is this block tri-diagonal matrix discretising the left-hand side of Eq. (32) and the boundary conditions, \mathbf{v} is a column vector containing the spectral coefficients e_{nk} and f_{nk} , and \mathbf{b} is a column vector containing all zeros, except for a single non-zero entry corresponding to the librational forcing term $e_1(1) = 1$. The NAG routines F07BRF and F07BSF

(https://www.nag.com/numeric/nl/nagdoc_24/nagdoc_f124/html/f07/f07brf.html and https://www.nag.com/numeric/nl/nagdoc_24/nagdoc_f124/html/f07/f07bsf.html) are then used to first compute the LU decomposition of \mathbf{A} , and then do the back-substitution to obtain the desired solution \mathbf{v} . In principle one could then do all numerical calculations with this code as just outlined. There are though two further improvements that were implemented.

First, the relationship $r = x$ was altered to $r = x + \delta(x - x^3)$. For $0 < \delta < 0.5$, this has the property of concentrating the Chebyshev collocation points even more toward the boundary at $r = 1$ than they naturally already are. It was found empirically that taking $\delta = 0.45$ allows the radial resolution K to be up to 30% less than the original $\delta = 0$ version, while still yielding identical results. The memory requirements to store the matrix \mathbf{A} scale as NK^2 , so reducing K by 30% allows a substantial increase in the angular resolution N , for a given core memory size.

The second code improvement is not about memory, but rather speed. In particular, we wish to compute very fine scans over the frequency range $\omega \in [0, 2]$, where we recall also that ω enters as a parameter in the matrix \mathbf{A} , since it appears in Eq. (32). Thus, having solved the problem for a given ω , if we then change ω by some tiny increment, do we really have to start all over, or can we somehow use the fact that we already have the LU decomposition of \mathbf{A} at the original frequency? To see how we can use this information, let \mathbf{A}_0 be the matrix at frequency ω_0 , and then consider the problem at frequency $\omega_0 + \Delta\omega$. Noting how ω enters Eq. (32), the new matrix will clearly be of the form $\mathbf{A}_0 + \Delta\omega \tilde{\mathbf{A}}$, where $\tilde{\mathbf{A}}$ is simply the discretized version of the term $i\mathbf{u}$. We, thus, wish to solve the problem

$$(\mathbf{A}_0 + \Delta\omega \tilde{\mathbf{A}})\mathbf{v} = \mathbf{b}, \quad (37)$$

and to do so in a way that uses the fact that we have already computed the LU decomposition of just \mathbf{A}_0 itself. This is accomplished by moving the $\Delta\omega \tilde{\mathbf{A}}\mathbf{v}$ term to the right, and then iterating according to

$$\mathbf{A}_0 \mathbf{v}^{(n+1)} = \mathbf{b} - \Delta\omega \tilde{\mathbf{A}} \mathbf{v}^{(n)}. \quad (38)$$

The final procedure is thus as follows: first compute the LU decomposition of \mathbf{A}_0 , corresponding to some frequency ω_0 . This is accomplished using NAG routine F07BRF, and becomes computationally very expensive at high resolutions, scaling as NK^3 . Next iterate according to Eq. (38), and for some $\pm\Delta\omega$ range centered around ω_0 . Each iteration is accomplished using NAG routine F07BSF and is computationally much cheaper, scaling only as NK^2 . How large $|\Delta\omega|$ can be taken before the iteration fails to converge, and a new LU decomposition corresponding to a new ω_0 has to be computed, is determined by simply trying it out. It was found that each of the peaks and troughs seen in the figures to follow typically required a few ω_0 values, but once the corresponding LU decompositions had been computed, this iterative solution method then allowed the precise details of the curves to be mapped out in far greater detail at relatively little additional cost. The final result is then identical to what the original direct solver would have accomplished, but allows a very fine scan of ω for $\sim 1/30$ the CPU time that a separate LU decomposition at each new frequency would have required. Specifically, at the highest resolutions, the factor of K saved by an iteration (NK^2) vs a new LU decomposition (NK^3) means that the iterative procedure is far faster, even if on average a dozen or so iterations might be required for each value of $\Delta\omega$.

With these improvements in place, the code was then run at resolutions $N \times K = 80 \times 170$ for Ekman number $E \geq 10^{-8}$, 100×270 for $E = 10^{-9}$, and 130×430 for $E = 10^{-10}$, where according to Eqs. (34) and (35), the maximum spherical harmonic degree is then $2N$ in each case. Recall also that the memory requirements scale as NK^2 and the CPU time for each LU decomposition scales as NK^3 . As E is reduced, this iterative procedure (38) also converges for increasingly small $|\Delta\omega|$ ranges as the peak/trough structures become increasingly narrow, thus requiring more and more LU decompositions to map out a given ω interval. The overall computational effort, therefore, increases even more rapidly than NK^3 . The final result is that $E \geq 10^{-8}$ is quite straightforward on a standard PC, $E = 10^{-9}$ still fits on a PC in terms of memory, but requires considerably more CPU time, whereas $E = 10^{-10}$ requires a machine with larger memory, and becomes so CPU-intensive that only a small fraction of the full range $\omega \in [0, 2]$ could be scanned.

V. RESULTS

A. Frequency response and flow structure

Figures 3 and 4 show the time-averaged kinetic energy $E_{num}/\varepsilon_{\phi,0}^2$ as a function of the libration frequency ω . The upper panels in each

figure show scans over the entire frequency range $\omega \in [0, 2]$, computed with a spacing $\Delta\omega = 2 \times 10^{-3}$, and down to Ekman numbers $E = 10^{-8}$. The lower panels zoom in on subsets covering only 1/10 of the full frequency range and include even smaller Ekman numbers on those subsets. In both figures, we observe a complicated series of peaks and troughs and exhibiting finer and finer structures for smaller E . As E is reduced the values at the peaks become independent of E , in agreement with the previous theoretical analysis; the main peaks can also be associated with some of the inertial modes given in Tables I and II.

In contrast, at the troughs between the peaks, the energies scale as $E^{1/2}$. Some of the most prominent troughs are also seen to correspond to the frequencies $\omega = 2 \sin(\pi/n)$ for integer n , for which the internal shear layers form particularly simple reflection patterns (periodic orbits). The upper panels in Figs. 3 and 4 indicate these frequencies for $n = 3, \dots, 10$.

For longitudinal libration, all of these values correspond to troughs, but for latitudinal libration, some of them are actually peaks. For example, $\omega = 1$ is the $n = 6$ reflection pattern, but according to Table II is also one of the resonant modes (the spin-over mode in this case). In cases such as this the resonant mode behavior dominates, and the result is a peak rather than a trough.

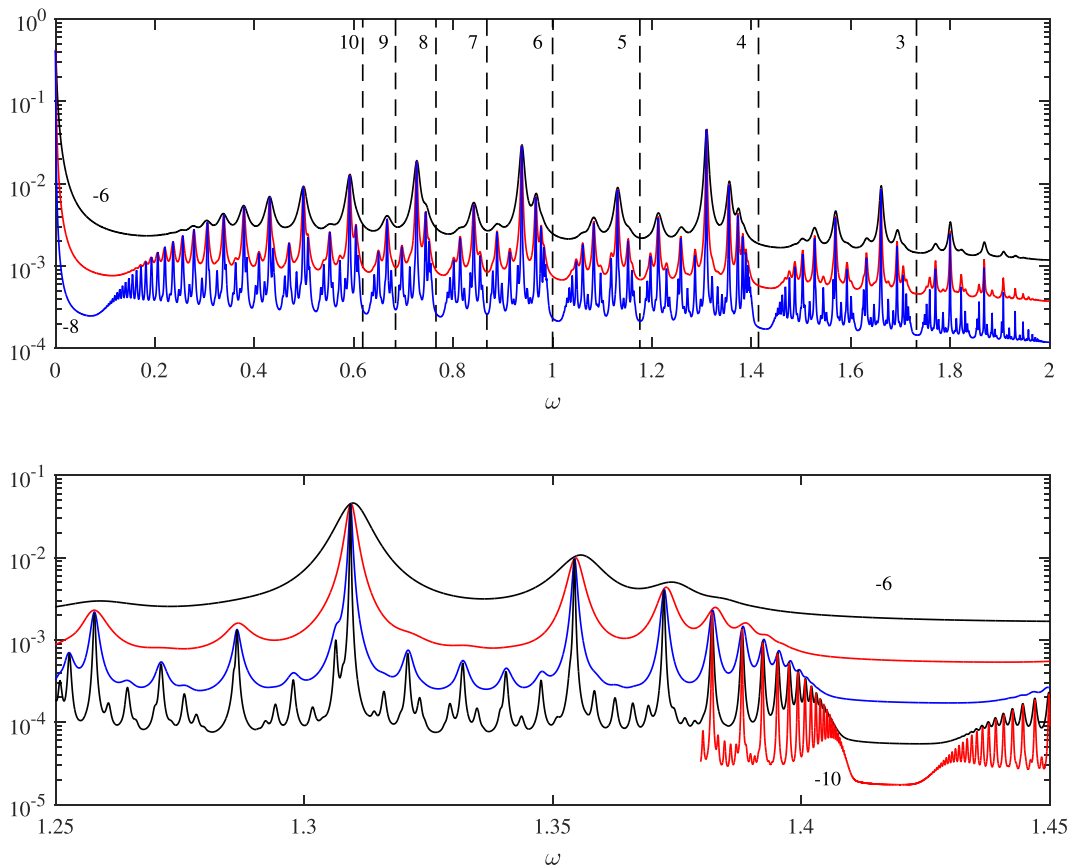


FIG. 3. The kinetic energy $E_{num}/\varepsilon_{\phi,0}^2$, averaged over the libration period, for the longitudinal libration case. The upper panel shows results for Ekman numbers $E = 10^{-6}, 10^{-7}, 10^{-8}$, as indicated by the labels -6 and -8 beside two of the curves. The lower panel shows details in the range $\omega \in [1.25, 1.45]$, with additional results for $E = 10^{-9}, 10^{-10}$. The dashed vertical lines in the upper panel are at frequencies $\omega = 2 \sin(\pi/n)$, with $n = 3, \dots, 10$ as indicated beside each line.

25 July 2023 14:54:50

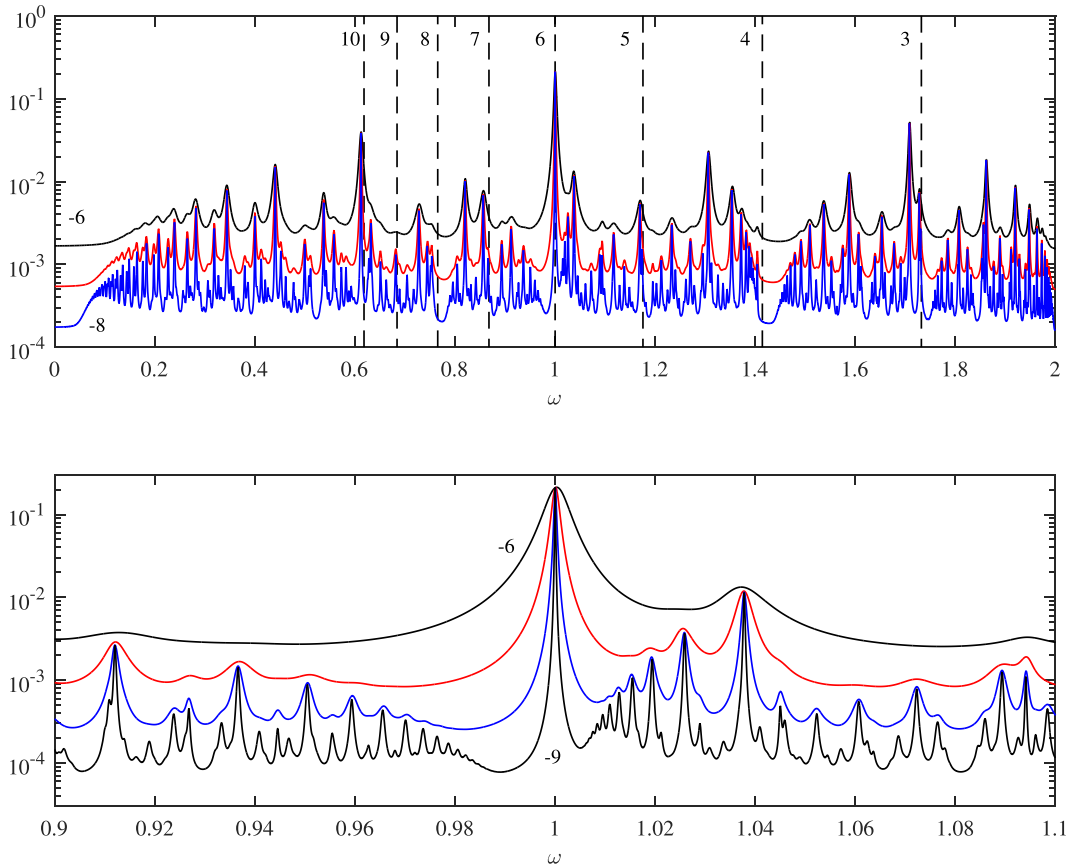


FIG. 4. The kinetic energy E_{num}/v_0^2 , averaged over the libration period, for the latitudinal libration case. The upper panel shows results for Ekman numbers $E = 10^{-6}, 10^{-7}, 10^{-8}$, as indicated by the labels -6 and -8 beside two of the curves. The lower panel shows details in the range $\omega \in [0.9, 1.1]$, with additional results for $E = 10^{-9}$. The dashed vertical lines in the upper panel are at frequencies $\omega = 2 \sin(\pi/n)$, with $n = 3, \dots, 10$ as indicated beside each line.

The other striking feature about Figs. 3 and 4 is how more and more peaks emerge as the Ekman numbers are reduced. Indeed, the pattern appears to be fractal: if we compare $E = 10^{-7}$ in the top rows with $E = 10^{-9}$ in the bottom rows, and temporarily ignoring different ω ranges, the curves are qualitatively very similar. If we then recall that the frequency ranges in the bottom rows are in each case 1/10 of the full ranges in the top rows, this suggests $E^{1/2}$ as the self-similarity

factor. Figure 5 further quantifies this by showing the distributions of the distance between two consecutive peaks, $(\omega_{n+1} - \omega_n)$, re-scaled by $E^{1/2}$. The fact that distributions for different Ekman numbers collapse on top of one another confirms that $E^{1/2}$ is the correct self-similarity factor. In the limit $E \rightarrow 0$, the entire interval $\omega \in [0, 2]$ would then become densely filled with peaks but always also still containing troughs between the peaks.

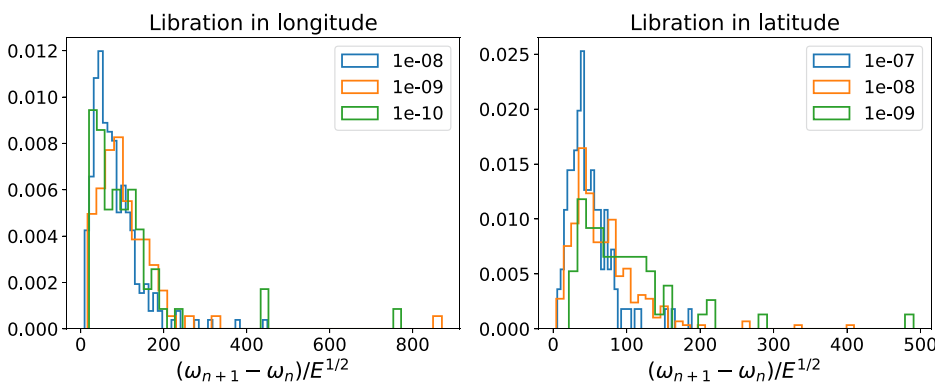


FIG. 5. Distribution of peak intervals re-scaled by $E^{1/2}$, with longitudinal libration (data from Fig. 3) on the left and latitudinal libration (data from Fig. 4) on the right. In each case only the lowest three Ekman numbers are shown.

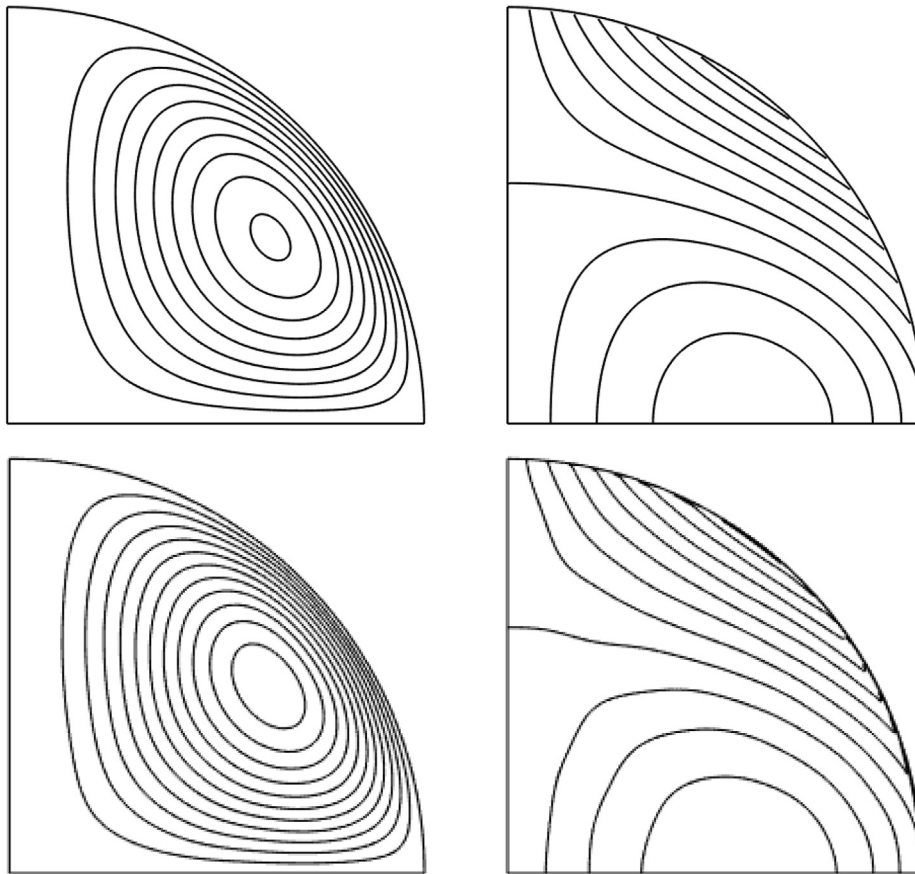


FIG. 6. The top row shows the theoretical mode profiles for the inertial mode with $(m, l, k) = (0, 4, 1)$ and $\omega_{mlk} = \sqrt{12/7} = 1.309$. Displayed are contours of the azimuthal velocity component u_ϕ (left) and streamlines of the meridional flow (right). The bottom row shows the corresponding numerical results for longitudinal libration at this frequency, and $E = 10^{-10}$.

Returning briefly to the peaks, we saw previously that the numerically computed energies are in excellent agreement with some of the theoretical values for the inertial modes in Tables I and II. Figure 6 shows an example illustrating that the corresponding spatial structures are also in near-perfect agreement with the theoretical mode profiles given by expressions (A5)–(A7). The top row shows the $(m, l, k) = (0, 4, 1)$ free eigenmode (which by itself has an arbitrary amplitude) matched up with the forced librational response at its frequency $\omega_{mlk} = \sqrt{12/7}$ in the bottom row. If the amplitude of the free mode is suitably adjusted, the two are seen to be virtually identical, confirming that the libration is indeed picking out this particular free mode.

Regarding the troughs, these are (relatively large) frequency bands with no inertial mode resonances at a given Ekman number. In these regions, the velocity field is dominated by conical shear layers emanating from the critical latitudes making an angle $\theta = \arcsin(\omega/2)$ with the vertical axis. As an example, we show results for longitudinal libration at $\omega = 2 \sin(\pi/8) = 0.765$ in Fig. 7. As explained in the study by Rieutord *et al.*,³⁴ for frequencies of the form $\omega = 2 \sin(\pi q)$, with q a rational number, the ray patterns of the inertial waves form periodic orbits, which has the consequence that regular inviscid inertial modes, in general, do not exist at these frequencies. Therefore, no inertial mode would be excited at these particular frequencies in the limit of vanishing viscosity, hence explaining the

troughs. The detailed scalings within these conical shear layers were also predicted by Stewartson and Roberts,³⁵ with the thickness scaling as $E^{1/5}$ and their characteristic velocities as $E^{1/5}$. By examining cuts along the blue line in Fig. 7, we obtained results in excellent agreement with these scalings.

Note finally that all the features obtained in this section confirm the theoretical inviscid spectrum predicted by Fig. 2 of Aldridge and Toomre.⁶

B. Convergence toward the asymptotic regime

Although numerical simulations such as the ones performed here allow us to compute Ekman numbers as small as 10^{-10} , the values in planetary cores can be several orders of magnitude smaller still, as small as $O(10^{-15})$. In this section, we therefore quantify the convergence of the asymptotic model as we decrease the Ekman number.

In Fig. 8, we show the frequency-shift of the peak corresponding to the resonance with the modes (0,8,3) and (1,2,1) excited by librations in longitude and latitude, respectively. The numerical results (full-circles) converge toward the asymptotic values $\omega_{lmk} + S_{lmk}E^{1/2}$ proposed by Greenspan.²⁶ For all peaks in Tables I and II, we next compute the residual errors between the numerical values ω_{num} and the asymptotic values, that is, we evaluate the quantity $\Delta\omega_{lmk} = \omega_{num} - \omega_{lmk} - S_{lmk}E^{1/2}$.

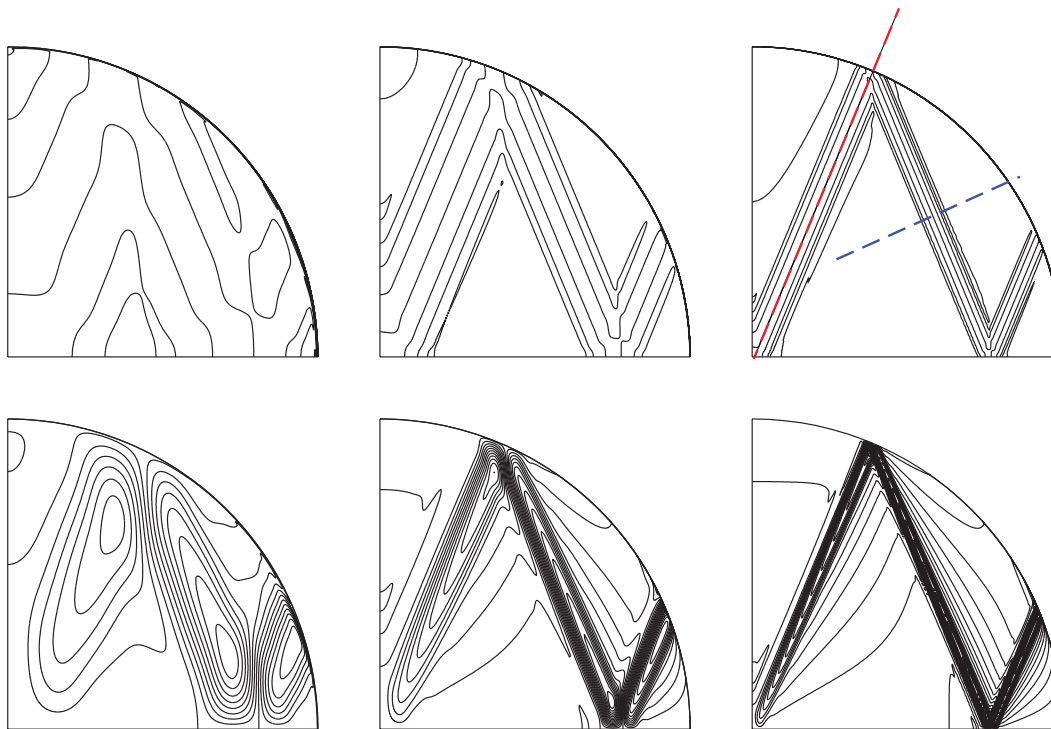


FIG. 7. Meridional cut of numerically obtained velocity profiles for the linear response to longitudinal libration at $\omega = 2 \sin(\pi/8) = 0.765$. Displayed are contours of the azimuthal velocity component u_ϕ (top) and streamlines of the meridional flow (bottom) for $E = 10^{-6}$ (left), $E = 10^{-8}$ (center), and $E = 10^{-10}$ (right). The red line indicates the theoretically predicted obliquity of the shear layers; the blue line shows the line along which asymptotic scalings were confirmed.

25 July 2023 14:54:50

As shown in Fig. 9, these errors are bounded by $\Delta\omega_{lmk} < O(E)$, as expected from the theory proposed by Greenspan.²⁶

The second quantity that an asymptotic model will allow us to estimate in the case of a resonance at planetary settings is the kinetic

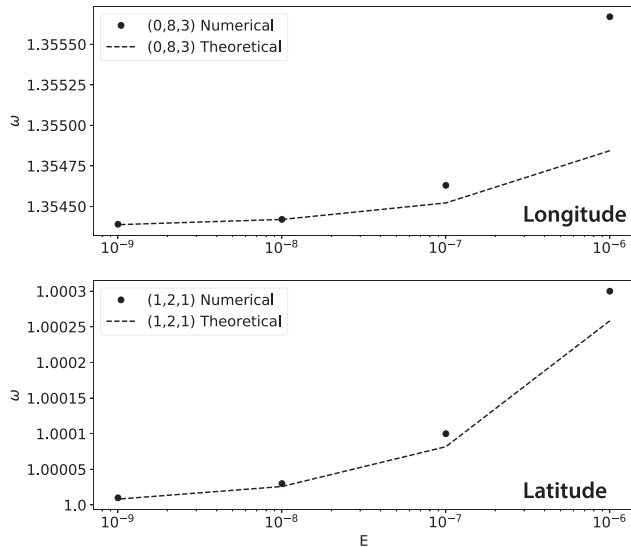


FIG. 8. Frequency of the peak associated with the eigenmodes (0,8,3) and (1,2,1) excited by librations in longitude (upper) and latitude (lower), respectively. The full-circles correspond to the numerical simulations, the dashed lines to the asymptotic results $\omega_{lmk} + S_{lmk}E^{1/2}$ from Tables I and II, respectively.

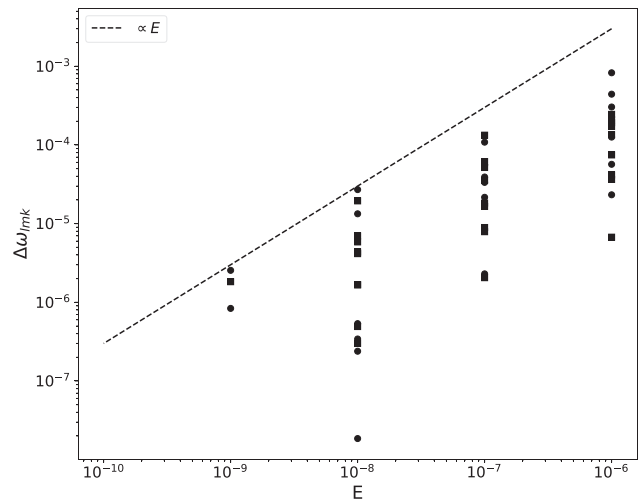


FIG. 9. The residual frequency errors $\Delta\omega_{lmk} = \omega_{num} - \omega_{lmk} - S_{lmk}E^{1/2}$, for several peaks of the libration in longitude (full-circle) and latitude (square), as functions of the Ekman number.

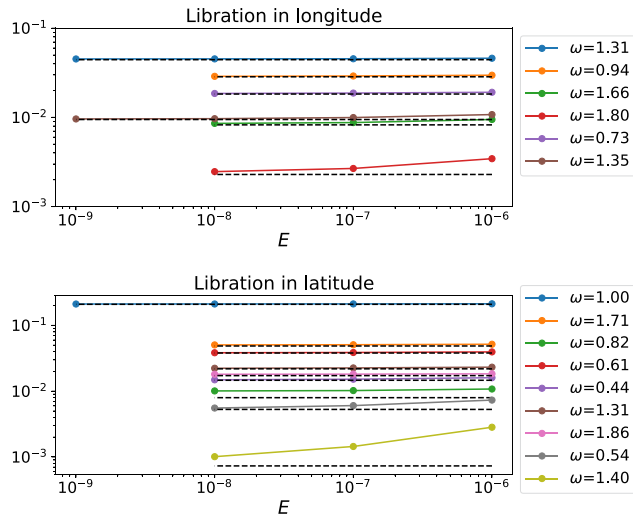


FIG. 10. Normalized kinetic energy, $E_{num}/\epsilon_{\phi,0}^2$, as a function of the Ekman number for the dominant peaks in Figs. 3 and 4. The black dashed lines represents the asymptotic values for the modes in Tables I and II for libration in longitude (top panel) and latitude (bottom panel), respectively.

energy, from which one can derive a typical rms velocity, $U = \sqrt{E_{kin}}$. From a theoretical standpoint we expect the amplitude of the peaks in the energy spectrum to be Ekman independent in the asymptotic regime, except for small contributions from the boundary layer at $O(E^{1/2})$ and the interior conical shear layers at $O(E^{3/5})$. In Fig. 10, we compare the energy at the peak frequencies from our numerical simulations with the asymptotic values in Tables I and II for libration in longitude and latitude, respectively. As before for the frequency, we observe a good quantitative agreement between the numerical simulations and the asymptotic model, even at moderate values of the Ekman number for the large-scale modes, having small l, k values.

C. The trough regions

We now focus on the trough regions introduced in Sec. V A, where no resonant modes are excited, and the low-energy flow instead

resembles the periodic orbit corresponding to the particular frequencies $\omega = 2 \sin(\pi q)$, with q a rational number. The trough regions cannot be captured by the asymptotic model as they correspond to flows driven by the boundary layer critical latitude, thus requiring a small but finite Ekman number. As we showed in Fig. 5, the distribution of the distance between peaks is at first order self-similar when rescaled by $E^{1/2}$, from which one might conjecture that the width of the troughs would also follow the same scaling. We shall see this is not the case though.

We define a trough in our numerical spectrum as the region around one of the frequencies associated with a periodic orbit bounded by the two nearest peaks, as shown in Fig. 11 for $\omega = \sqrt{2}$. The nearest peaks at ω_- and ω_+ define the width of the trough as $\delta = |\omega_+ - \omega_-|$. The characteristic energy of a trough is defined at the central frequency $f = \frac{1}{2}(\omega_+ + \omega_-)$, indicated by the red circles in the left panel of Fig. 11. We perform the same analysis for all the troughs near the frequencies of the periodic orbits represented by vertical lines in Figs. 3 and 4.

For each trough, we fit a power law using linear regression in log–log space for the width and energy, $\delta \propto E^\alpha$ and $E_{num}/\epsilon_{\phi,0}^2 \propto E^\beta$, respectively. Figure 12 shows the distribution of the exponents for the width and energy scaling laws for all periodic orbit troughs driven by longitudinal and latitudinal librations. Quite clearly, the energy scales as $E^{1/2}$, consistent with an energy dominated by the flow in the Ekman boundary layer $E_{num}/\epsilon_{\phi,0}^2 \propto E^{1/2}$ with an additional smaller contribution from the conical shear layers in the bulk contributing at the order $E^{3/5}$.

What is more surprising is the scaling of the width $\delta \propto E^{0.23 \pm 0.05}$, close to $E^{1/4}$. Indeed, from the self-similar distribution of the distance between peaks re-scaled by $E^{1/2}$ (see Sec. V A), one would have guessed that the width of the troughs should also follow the same scaling. However, one should note that the widest troughs correspond to the tails of the distributions in Fig. 5, which do not exhibit any self-similarity when re-scaled by $E^{1/2}$. To the best of our knowledge there is no theory that explains these observations regarding the widths of the trough regions.

In Fig. 13, we collapse the longitudinal libration energy spectra in the vicinity of the trough at $\omega_t = \sqrt{2}$. That is, we rescale the energy by $E^{1/2}$, and the frequency as $(\omega - \omega_t)/E^{0.23}$. The troughs for the three different values $E = 10^{-8}, 10^{-9}, 10^{-10}$ are seen to almost completely

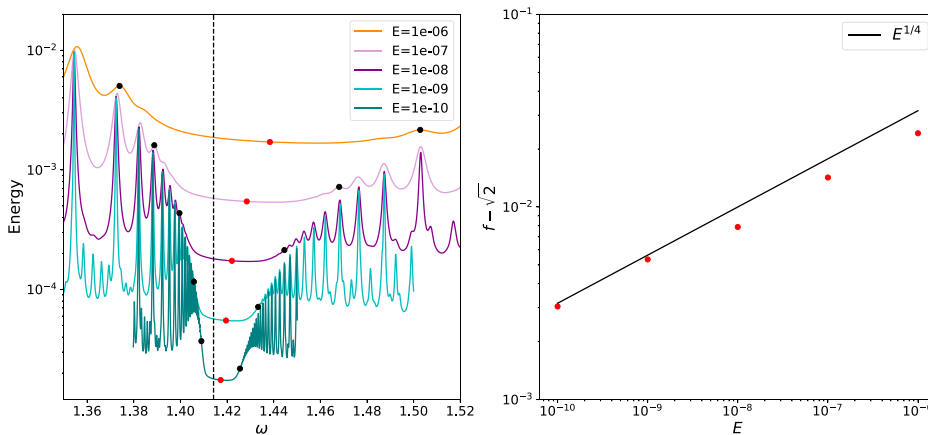


FIG. 11. The left panel shows the kinetic energy $E_{num}/\epsilon_{\phi,0}^2$ for longitudinal libration in the vicinity of the periodic orbit frequency $\omega = \sqrt{2}$, indicated by dashed vertical line. The black circles correspond to the nearest peaks and define the width of the trough; the central frequency f is represented by the red circle. The right panel shows how this central frequency converges toward the periodic orbit frequency as E is reduced; the scaling is seen to be $(f - \sqrt{2}) \propto E^{1/4}$.

25 July 2023 14:54:50

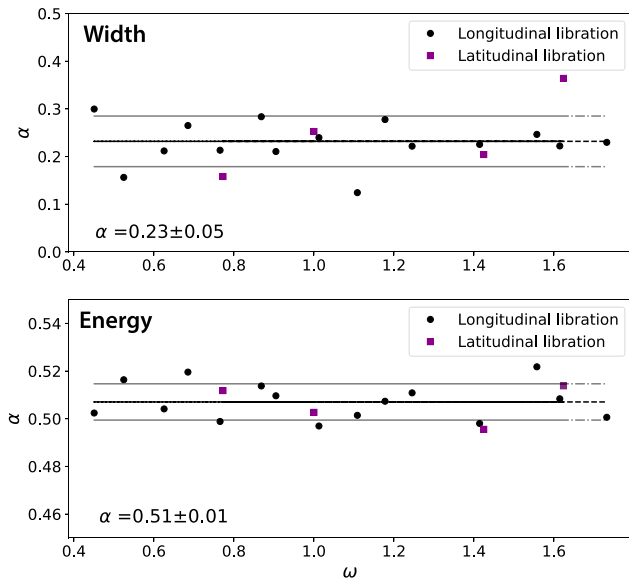


FIG. 12. Exponents of the best scaling laws for the width $\delta \propto E^\alpha$ (top) and the energy at the central frequency $E_{num}/\epsilon_{\phi,0}^2 \propto E^\alpha$. The mean value of each exponent and its standard deviation is indicated in the respective panel.

coincide under these rescalings. Similar collapsing is observed for all the troughs, whether driven by libration in longitude or in latitude.

VI. CONCLUSIONS AND PERSPECTIVES

We have used asymptotics and numerics to systematically study libration in both longitude and latitude in a rotating, fluid-filled sphere. The asymptotic theory allows a clear prediction of the resonant eigenmodes, in agreement with previous studies for longitudinal libration by Zhang and Liao,²⁷ which form a dense set on the frequency interval $\omega \in [0, 2]$. Including the first-order viscous correction to the eigenfrequencies, $\omega = \omega_{mk} + S_{mk}E^{1/2}$ yields results that are then always within $O(E)$ of the corresponding numerical results. This indicates that extrapolation to Ekman numbers found in planetary settings, with Ekman numbers as small as $E = O(10^{-15})$, is possible with very high accuracy.

For increasingly small Ekman numbers, the numerically computed frequency response tends toward a fractal structure, with

increasingly finely spaced peaks and troughs. The energies at the peaks become independent of E , a well-known results in spheres;²⁷ they correspond to resonant conditions of eigenmodes. The energies at the troughs scale as $E^{1/2}$, and correspond to frequencies where the internal reflection patterns form periodic orbits. The fractal self-similarity factor for the spacing between the peaks is $E^{1/2}$ in general, but the self-similarity factor for the widths of the widest troughs is $E^{-0.23} \sim E^{1/4}$. An asymptotic theory that explains these aspects of the fractal pattern, and especially why peaks and troughs have different self-similarity factors, does not yet exist, but would certainly be of considerable interest.

Librations arise mainly in tidally locked satellites such as the Earth’s moon, Callisto, Ganymede, Io and Titan, for which the main librations are at $\omega = 1$. For those satellites with equatorial [$\xi_{eq} = \sqrt{(a^2 - b^2)}/a^2$] and polar [$\xi_{pol} = \sqrt{(a^2 - c^2)}/a^2$] ellipticity small with respect to $E^{1/4}$ (Refs. 23 and 36), our spherical theory provides a realistic estimate of the velocities. Note that here we adopt the convention of Zhang and Liao;²⁷ other conventions exist in the literature leading to different inequalities, for instance adopting the conventions of Grannan *et al.*¹⁹ [$\beta = |a^2 - b^2|/(a^2 + b^2)$] or the polar flattening $\eta = (a - b)/a$ (Refs. 37 and 38) the condition becomes $\beta, \eta \ll E^{1/2}$. For finite ellipticities, i.e., in true ellipsoids, longitudinal librations still do not lead to direct resonances of any inertial modes, resulting in amplitudes scaling comparable to what is obtained in the full sphere, see Ref. 27 for more details. In contrast, for latitudinal librations, a finite polar flattening will result in a pressure coupling leading to a scaling of the spin-over mode amplitude proportional to $\Delta\theta/E^{1/2}$ (Refs. 25 and 27) near its resonant frequency, i.e., $|\omega - 2/(2 - \xi_{pol}^2)| \ll O(E^{1/2})$, potentially very large at planetary settings. Meanwhile, for all other frequencies, it has been shown that latitudinal librations cannot resonate with any inertial mode,²³ similarly to what is found for precession.³⁹

A detailed application of our results to any particular celestial object and specific libration frequency would require an extensive discussion of the validity of the assumptions underlying our model, which is beyond the scope of this study. However, one can estimate an order of magnitude of the velocity at the peaks in typical planetary settings. To do so, we shall use a core radius $R = 500$ km, a rotation period of 1 day and a libration amplitude $\epsilon \sim 10^{-4}$. A typical velocity is obtained from our Tables I and II as $U_{rms} = \epsilon\Omega R\sqrt{(E_{mk}/\epsilon^2)/(4\pi/3)}$ leading to motions in the sub-mm/s range.

Including an inner core remains analytically challenging as the inertial modes in a spherical shell form an ill-posed mathematical

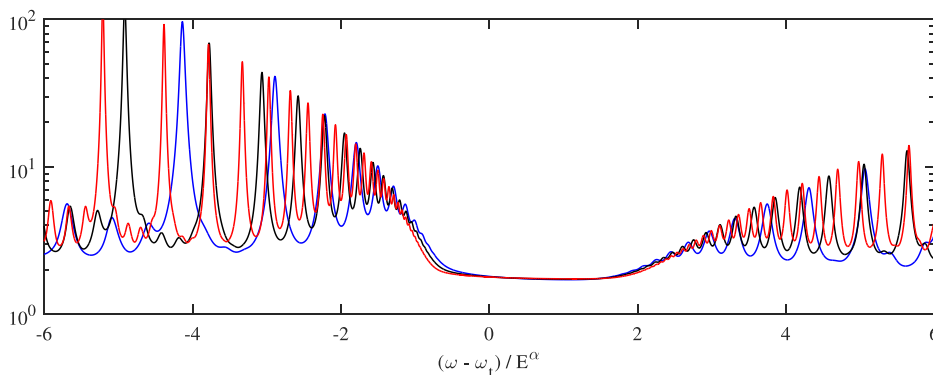


FIG. 13. The rescaled kinetic energy $(E_{num}/\epsilon_{\phi}^2)/E^{1/2}$ on the vertical axis vs the rescaled frequency on the horizontal axis, for Ekman numbers 10^{-8} (blue), 10^{-9} (black), and 10^{-10} (red). The frequency is centered on the periodic orbit frequency $\omega_t = \sqrt{2}$ and re-scaled by E^α with $\alpha = 0.23$.

problem.³⁴ Our approach could be extended to include an inner shell and provide an efficient way to scrutinize the linear response induced by the librations in a spherical shell at low Ekman numbers.⁴⁰

ACKNOWLEDGMENTS

Y.L. was supported by NSFC grants (Nos. 42174215 and 12250012) and the National Key R&D Program of China (No. 2022YFF0503200). R.H. was supported by STFC Grant Nos. ST/S000275/1 and ST/W000873/1. R.H. also thanks the Isaac Newton Institute for Mathematical Sciences, Cambridge, for support and hospitality during the programme “Frontiers in dynamo theory: from the Earth to the stars” where work on this paper was undertaken. This work was supported by EPSRC Grant No. EP/R014604/1. R.H.’s visit to the Newton Institute was supported by a grant from the Heilbronn Institute. J.N. was supported by SNSF Grant Nos. 200021_140708 and 200021_185088. J.N. and S.V. are grateful for the provision of computing resources by the Swiss National Supercomputer Centre (CSCS) under allocation s1111. J. N. would like to dedicate this paper to Dr. Hugo Perfettini for 30 years of loyal friendship.

AUTHOR DECLARATIONS

Conflict of Interest

The authors have no conflicts to disclose.

Author Contributions

Yufeng Lin: Conceptualization (equal); Formal analysis (equal); Writing – original draft (equal); Writing – review & editing (equal). **Rainer Hollerbach:** Conceptualization (equal); Formal analysis (lead); Writing – original draft (equal); Writing – review & editing (equal). **Jerome Noir:** Conceptualization (equal); Formal analysis (equal); Writing – original draft (equal); Writing – review & editing (equal). **Stijn Vantieghem:** Conceptualization (equal); Formal analysis (lead); Writing – original draft (equal).

DATA AVAILABILITY

The data that support the findings of this study are available from the corresponding author upon reasonable request.

APPENDIX A: INERTIAL MODES IN A SPHERE

The normal modes of wave propagation in an inviscid fluid are of the form $\mathbf{u} = \mathbf{u}_{lmk} \exp(i\omega_{lmk} t)$, where $\{\omega, \mathbf{u}, p\}$ are solutions of the eigenvalue problem

$$i\omega \mathbf{u} + 2\hat{\mathbf{z}} \times \mathbf{u} + \nabla p = 0 \tag{A1}$$

together with the incompressibility condition $\nabla \cdot \mathbf{u} = 0$ and the boundary condition $\mathbf{u} \cdot \hat{\mathbf{n}} = 0$. Solutions to this problem have been well-documented in the literature.^{26,41,42} There is an infinite set of eigenvalues ω_{lmk} , which are the real roots of the transcendental equation,

$$mP_l^{|m|}\left(\frac{1}{2}\omega\right) = \left(1 - \frac{1}{4}\omega^2\right) \frac{d}{d\omega} P_l^{|m|}\left(\frac{1}{2}\omega\right), \tag{A2}$$

where $P_l^{|m|}$ are the associated Legendre functions of degree l and order m . For each combination of $l > 0, -l \leq m \leq l$, the characteristic equation (A2) has a finite number of zeros. Hence, we can label each mode by an integer triplet $\{l, m, k\}$. The corresponding pressure eigenfunction is given by

$$p_{lmk} = \Psi_{kl}(s, z) \exp(im\phi) = \left\{ \prod_{n=1}^N \left[\eta_n^2 \left(1 - \frac{\omega_{lmk}^2}{4}\right) s^2 + \frac{\omega_{lmk}^2}{4} (1 - \eta_n^2) z^2 + \eta_n^2 (\eta_n^2 - 1) \right] \right\} \times \exp(im\phi), \tag{A3}$$

where (s, ϕ, z) are cylindrical coordinates and $\eta_n (n = 1, \dots, N)$ denotes one of the real distinct zeros of $P_l^{|m|}$ on the open interval $(0, 1)$. On the surface of the sphere $r = 1$, the pressure eigenmode takes the form

$$p_{lmk} = P_l^{|m|} \exp(im\phi) \tag{A4}$$

up to some arbitrary multiplicative constant.

Once the pressure eigenfunction is known, the velocity can be computed as (see Greenspan,²⁶ Eq. 2.7.2)

$$\mathbf{u}_{lmk} = -\frac{i}{4 - \omega_{lmk}^2} \left(\omega_{lmk} \frac{\partial \Psi_{kl}}{\partial s} + \frac{2m}{s} \Psi_{kl} \right) \exp(im\phi) \hat{\mathbf{s}} \tag{A5}$$

$$+ \frac{1}{4 - \omega_{lmk}^2} \left(2 \frac{\partial \Psi_{kl}}{\partial s} + \frac{m\omega_{lmk}}{s} \Psi_{kl} \right) \exp(im\phi) \hat{\phi} \tag{A6}$$

$$+ \frac{i}{\omega_{lmk}} \frac{\partial \Psi_{kl}}{\partial z} \exp(im\phi) \hat{\mathbf{z}}. \tag{A7}$$

Finally, inertial modes also satisfy an orthogonality property, i.e., if $\omega_{lmk} \neq \omega_{l'm'k'}$, then

$$\iiint \mathbf{u}_{lmk} \cdot \mathbf{u}_{l'm'k'}^\dagger dV = \delta_{ll'} \delta_{mm'} \delta_{kk'}. \tag{A8}$$

APPENDIX B: SOLUTION OF THE BOUNDARY LAYER EQUATIONS

In this appendix, we derive the boundary layer flow $\tilde{\mathbf{u}}$ that matches a given interior flow \mathbf{u}_0 to a boundary condition \mathbf{u}_Σ of the form (10) and (11). Following the discussion in Sec. III, the libration frequency ω lies within the inertial mode spectrum $\omega \in [0, 2]$ and the leading-order interior flow is taken to be of the form $\mathbf{u}_0 = A_{lmk} \mathbf{u}_{lmk}$ with \mathbf{u}_{lmk} an inertial mode whose eigenfrequency is ω .

The basic premises of boundary layer theory are (1) that the viscous force is negligible everywhere except in the vicinity of the boundary, and (2) that, within the boundary layer, variations in wall-normal direction are much larger than lateral ones, i.e., $\partial_r \gg r^{-1} \partial_\theta, r^{-1} \partial_\phi$. It is customary to introduce a boundary layer coordinate $\xi = 1 - E^{-1/2} r$. The divergence constraint can then be written as follows:

$$-E^{-1/2} \frac{1}{r^2} \frac{\partial}{\partial \xi} (r^2 \tilde{u}_r) + \frac{1}{r^2 \sin \theta} \frac{\partial}{\partial \theta} (\sin \theta \tilde{u}_\theta) + \frac{1}{r^2 \sin^2 \theta} \frac{\partial \tilde{u}_\phi}{\partial \phi} = 0. \tag{B1}$$

The last two terms on the right-hand side of this expression are $O(1)$, and this implies that \tilde{u}_r is $O(\sqrt{E})$. Thus, the leading-order term of the corrective velocity $\tilde{\mathbf{u}}$ is purely tangential.

These results allow us to recast the momentum equation for the $\tilde{\mathbf{u}}$ as follows:

$$i\omega \tilde{\mathbf{u}} + 2\hat{\mathbf{z}} \times \tilde{\mathbf{u}} - \frac{\partial \tilde{p}}{\partial \xi} \hat{\mathbf{r}} = \frac{\partial^2}{\partial \xi^2} \tilde{\mathbf{u}}. \quad (\text{B2})$$

We can now eliminate the pressure gradient by taking the vector product of the above equation with $\hat{\mathbf{r}}$,

$$i\omega (\tilde{\mathbf{u}} \times \hat{\mathbf{r}}) + 2 \cos \theta \tilde{\mathbf{u}} = \frac{\partial^2}{\partial \xi^2} (\tilde{\mathbf{u}} \times \hat{\mathbf{r}}). \quad (\text{B3})$$

Given that $\hat{\mathbf{r}} \times (\tilde{\mathbf{u}} \times \hat{\mathbf{r}}) = \tilde{\mathbf{u}}$ at the leading order, the vector product of $\hat{\mathbf{r}}$ with the above equation yields

$$i\omega \tilde{\mathbf{u}} - 2 \cos \theta \tilde{\mathbf{u}} \times \hat{\mathbf{r}} = \frac{\partial^2}{\partial \xi^2} \tilde{\mathbf{u}}. \quad (\text{B4})$$

Combining (B3) and (B4) eventually leads to a fourth-order differential equation for $\tilde{\mathbf{u}}$,

$$\left(\frac{\partial^2}{\partial \xi^2} - i\omega \right)^2 \tilde{\mathbf{u}} + 4 \cos^2 \theta \tilde{\mathbf{u}} = 0. \quad (\text{B5})$$

This fourth-order equation should be equipped with four boundary conditions. First, we prescribe that the no-slip boundary condition should be satisfied at the surface $r = 1$, i.e.,

$$\tilde{\mathbf{u}} + A_{lmk} \mathbf{u}_{lmk} - \mathbf{u}_\Sigma = 0. \quad (\text{B6})$$

Finally, we also require that the boundary layer flow vanishes exponentially at the outer edge of the boundary layer, i.e.,

$$\lim_{\xi \rightarrow \infty} \tilde{\mathbf{u}} = 0, \quad (\text{B7})$$

$$\lim_{\xi \rightarrow \infty} \frac{\partial^2 \tilde{\mathbf{u}}}{\partial \xi^2} = 0. \quad (\text{B8})$$

The general solution of this equation can be written as

$$\tilde{\mathbf{u}} = \tilde{\mathbf{u}}_+ \exp(\gamma_+ \xi) + \tilde{\mathbf{u}}_- \exp(\gamma_- \xi) \quad (\text{B9})$$

with

$$\gamma_+ = -\frac{\sqrt{2}}{2} \left(1 + i \frac{\omega + 2 \cos \theta}{|\omega + 2 \cos \theta|} \right) |\omega + 2 \cos \theta|^{1/2}, \quad (\text{B10})$$

$$\gamma_- = -\frac{\sqrt{2}}{2} \left(1 + i \frac{\omega - 2 \cos \theta}{|\omega - 2 \cos \theta|} \right) |\omega - 2 \cos \theta|^{1/2}. \quad (\text{B11})$$

Imposing the two boundary conditions at $\xi = 0$ eventually gives

$$\tilde{\mathbf{u}}_+ = \frac{1}{2} (A_{lmk} (\mathbf{u}_{lmk} - i\hat{\mathbf{r}} \times \mathbf{u}_{lmk}) - (\mathbf{u}_\Sigma - i\hat{\mathbf{r}} \times \mathbf{u}_\Sigma)), \quad (\text{B12})$$

$$\tilde{\mathbf{u}}_- = \frac{1}{2} (A_{lmk} (\mathbf{u}_{lmk} + i\hat{\mathbf{r}} \times \mathbf{u}_{lmk}) - (\mathbf{u}_\Sigma + i\hat{\mathbf{r}} \times \mathbf{u}_\Sigma)). \quad (\text{B13})$$

It is noteworthy that there are two critical latitudes $\theta_c = \pm \arccos(\omega/2)$ for which the solution (23) becomes singular, and correspond to the locations from which internal shear layers emanate. Following Greenspan,²⁶ Kudlick,⁴³ these singularities can be ignored when computing the Ekman pumping.

REFERENCES

- ¹J. Vidal and D. Cébron, "Inviscid instabilities in rotating ellipsoids on eccentric Kepler orbits," *J. Fluid Mech.* **833**, 469–511 (2017).
- ²C. D. Murray and S. F. Dermott, *Solar System Dynamics* (Cambridge University Press, 1999).
- ³S. Vantighem, D. Cébron, and J. Noir, "Latitudinal libration driven flows in triaxial ellipsoids–corrigendum," *J. Fluid Mech.* **830**, 823–823 (2017).
- ⁴R. Poincaré, "Sur la précession des corps déformables," *Bull. Astr.* **27**, 321 (1910).
- ⁵H. Greenspan, "On the transient motion of a contained rotating fluid," *J. Fluid Mech.* **20**, 673–696 (1964).
- ⁶K. Aldridge and A. Toomre, "Axisymmetric inertial oscillations of a fluid in a rotating spherical container," *J. Fluid Mech.* **37**, 307–323 (1969).
- ⁷K. Zhang, K. Chan, X. Liao, and J. Aurnou, "The non-resonant response of fluid in a rapidly rotating sphere undergoing longitudinal libration," *J. Fluid Mech.* **720**, 212–235 (2013).
- ⁸J. Noir, F. Hemmerlin, J. Wicht, S. Baca, and J. Aurnou, "An experimental and numerical study of librationaly driven flow in planetary cores and subsurface oceans," *Phys. Earth Planet. Inter.* **173**, 141–152 (2009).
- ⁹M. Calkins, J. Noir, J. Eldredge, and J. Aurnou, "Axisymmetric simulations of libration-driven fluid dynamics in a spherical shell geometry," *Phys. Fluids* **22**, 086602 (2010).
- ¹⁰M. Rieutord, "Linear theory of rotating fluids using spherical harmonics. Part II, Time-periodic flows," *Geophys. Astrophys. Fluid Dyn.* **59**, 185–208 (1991).
- ¹¹A. Tilgner, "Driven inertial oscillations in spherical shells," *Phys. Rev. E* **59**, 1789–1794 (1999).
- ¹²F. Busse, "Mean zonal flows generated by librations of a rotating spherical cavity," *J. Fluid Mech.* **650**, 505 (2010).
- ¹³A. Sauret, D. Cébron, C. Morize, and M. Le Bars, "Experimental and numerical study of mean zonal flows generated by librations of a rotating spherical cavity," *J. Fluid Mech.* **662**, 260–268 (2010).
- ¹⁴S. Koch, U. Harlander, C. Egbers, and R. Hollerbach, "Inertial waves in a spherical shell induced by librations of the inner sphere: Experimental and numerical results," *Fluid Dyn. Res.* **45**, 035504 (2013).
- ¹⁵Y. Lin and J. Noir, "Libration-driven inertial waves and mean zonal flows in spherical shells," *Geophys. Astrophys. Fluid Dyn.* **115**, 258–279 (2021).
- ¹⁶D. Cébron, J. Vidal, N. Schaeffer, A. Borderies, and A. Sauret, "Mean zonal flows induced by weak mechanical forcings in rotating spheroids," *J. Fluid Mech.* **916**, A39 (2021).
- ¹⁷D. Cébron, M. Le Bars, J. Noir, and J. Aurnou, "Libration driven elliptical instability," *Phys. Fluids* **24**, 061703 (2012).
- ¹⁸C. Wu and P. Roberts, "On a dynamo driven topographically by longitudinal libration," *Geophys. Astrophys. Fluid Dyn.* **107**, 20 (2013).
- ¹⁹A. Grannan, M. Le Bars, D. Cébron, and J. Aurnou, "Experimental study of global-scale turbulence in a librating ellipsoid," *Phys. Fluids* **26**, 126601 (2014).
- ²⁰B. Favier, A. Grannan, M. Le Bars, and J. Aurnou, "Generation and maintenance of bulk turbulence by libration-driven elliptical instability," *Phys. Fluids* **27**, 066601 (2015).
- ²¹M. Le Bars, D. Cébron, and P. Le Gal, "Flows driven by libration, precession, and tides," *Annu. Rev. Fluid Mech.* **47**, 163–193 (2015).
- ²²M. L. Bars and D. Lecoanet, *Fluid Mechanics of Planets and Stars* (Springer, 2020).
- ²³K. Zhang, K. Chan, and X. Liao, "Asymptotic theory of resonant flow in a spheroidal cavity driven by latitudinal libration," *J. Fluid Mech.* **692**, 420–445 (2012).
- ²⁴K. H. Chan, X. Liao, and K. Zhang, "Simulations of fluid motion in spheroidal planetary cores driven by latitudinal libration," *Phys. Earth Planet. Inter.* **187**, 404–415 (2011).
- ²⁵S. Vantighem, D. Cébron, and J. Noir, "Latitudinal libration driven flows in triaxial ellipsoids," *J. Fluid Mech.* **771**, 193–228 (2015).
- ²⁶H. Greenspan, *The Theory of Rotating Fluids* (Cambridge University Press, 1968).
- ²⁷K. Zhang and X. Liao, *Theory and Modeling of Rotating Fluids: Convection, Inertial Waves and Precession* (Cambridge University Press, 2017).
- ²⁸D. Ivers, A. Jackson, and D. Winch, "Enumeration, orthogonality and completeness of the incompressible Coriolis modes in a sphere," *J. Fluid Mech.* **766**, 468–498 (2015).

25 July 2023 14:54:50

- ²⁹G. Backus and M. Rieutord, “Completeness of inertial modes of an incompressible non-viscous fluid in a corotating ellipsoid,” *Phys. Rev. E* **95**, 053116 (2017).
- ³⁰R. Hollerbach and R. Kerswell, “Oscillatory internal shear layers in rotating and precessing flows,” *J. Fluid Mech.* **298**, 327–339 (1995).
- ³¹R. Hollerbach, “Imposing a magnetic field across a nonaxisymmetric shear layer in a rotating spherical shell,” *Phys. Fluids* **6**, 2540–2544 (1994).
- ³²R. Hollerbach, C. Nore, P. Marti, S. Vantieghem, F. Luddens, and J. Leorat, “Parity-breaking flows in precessing spherical containers,” *Phys. Rev. E* **87**, 053020 (2013).
- ³³R. Hollerbach and G. Ierley, “A modal α^2 -dynamo in the limit of asymptotically small viscosity,” *Geophys. Astrophys. Fluid Dyn.* **56**, 133–158 (1991).
- ³⁴M. Rieutord, B. Georgeot, and L. Valdetaro, “Inertial waves in a rotating spherical shell: Attractors and asymptotic spectrum,” *J. Fluid Mech.* **435**, 103–144 (2001).
- ³⁵K. Stewartson and P. Roberts, “On the motion of a liquid in a spheroidal cavity of precessing rigid body,” *J. Fluid Mech.* **17**, 1–20 (1963).
- ³⁶K. Zhang, K. Chan, and X. Liao, “On fluid motion in librating ellipsoids with moderate equatorial eccentricity,” *J. Fluid Mech.* **673**, 468–479 (2011).
- ³⁷J. Noir, P. Cardin, D. Jault, and J. Masson, “Experimental evidence of non-linear resonance effects between retrograde precession and the tilt-over mode within a spheroid,” *Geophys. J. Int.* **154**, 407–416 (2003).
- ³⁸R. Kerswell, “The instability of precessing flow,” *Geophys. Astrophys. Fluid Dyn.* **72**, 107–144 (1993).
- ³⁹J. Vidal and D. Cébron, “Precession-driven flows in stress-free ellipsoids,” *J. Fluid Mech.* **954**, A5 (2023).
- ⁴⁰Y. Lin and G. I. Ogilvie, “Resonant tidal responses in rotating fluid bodies: Global modes hidden beneath localized wave beams,” *Astrophys. J. Lett.* **918**, L21 (2021).
- ⁴¹G. Bryan, “The waves on a rotating liquid spheroid of finite ellipticity,” *Philos. Trans. R. Soc. London, A* **180**, 187–219 (1889).
- ⁴²K. Zhang, P. Earnshaw, X. Liao, and F. Busse, “On inertial waves in a rotating fluid sphere,” *J. Fluid Mech.* **437**, 103–119 (2001).
- ⁴³M. Kudlick, “On transient motions in a contained, rotating fluid,” Ph.D. thesis (Massachusetts Institute of Technology, 1966).